Engineering Failure Analysis 46 (2014) 76–91

Contents lists available at ScienceDirect

Engineering Failure Analysis

journal homepage: www.elsevier.com/locate/engfailanal

Comparative performance of turbine blades used in power generation: Damage vs. microstructure and superalloy composition selected for the application

H.M. Tawancy *, Luai M. Al-Hadhrami

Center for Engineering Research, Research Institute, King Fahd University of Petroleum and Minerals, Box 1639, Dhahran 31261, Saudi Arabia

ARTICLE INFO

Article history:
Received 13 June 2014
Accepted 7 August 2014
Available online 15 August 2014

Keywords:
Turbine blades
Ni-base superalloys
Microstructure
Creep
Fatigue

ABSTRACT

First-stage turbine blades made of different grades of Ni-base superalloys and environmentally protected by the same Cr-modified aluminide coating are examined after exposure to the same service conditions in an electric power plant. Emphasis is placed upon microstructural changes, which can degrade the blade performance. Various electron-optical techniques are used to characterize the microstructures of unused and used blades. Three types of microstructural changes, which can lead to intergranular creep failure, are identified. These changes include: (i) coarsening, agglomeration, and rafting of the strengthening γ'-phase, (ii) formation of γ'-denuded zones alongside grain boundaries, and (iii) precipitation of intermetallic compounds. However, fatigue failure is also observed particularly in cases where higher than normal temperature is encountered. Although the same microstructural changes are found to occur in the blades included in the study, the respective kinetics appear to be influenced by at least two parameters: (i) exact superalloy composition and (ii) actual operating temperature. It is concluded that the life expectancy of blades used in such applications can be realized by appropriate selection of superalloy composition and adherence to design specifications.

1. Introduction

To meet the increasing demand for electric power and simultaneously conserve energy and maintain cleaner environment, designers are always motivated to operate industrial gas turbine engines at higher temperatures to achieve higher efficiency and more power output [1]. However, this goal is limited by the heat resistance of material systems used in the turbine section where the temperature reaches its maximum value during engine operation. Therefore, gas turbine design presents an example of a material-driven technology.

Due to the combination of high stresses and temperature encountered in the turbine section, mechanical strength including tensile, creep, and fatigue is the primary requirement, which is mostly satisfied by the superalloys [2–4]. However, because of the inadequate environmental resistance of bare superalloys, the surface integrity of the blades is maintained by protective coatings such as Cr-modified aluminides, Pt-aluminides, and overlays of the MCrAlY-type (M stands for Ni or Ni + Co) [5–7].

* Corresponding author. Tel.: +966 013 8604317; fax: +966 013 8603996.
E-mail address: tawancy@kfupm.edu.sa (H.M. Tawancy).

http://dx.doi.org/10.1016/j.engfailanal.2014.08.007
1350-6307/

Qualitatively, the microstructural features of Ni-base superalloys prior to service are rather similar [4]. Each alloy consists of a fine dispersion of the strengthening γ′-phase based upon the Ni_3Al composition (ordered cubic $L1_2$ superlattice) in a matrix of γ-phase (Ni-rich solid-solution) with face-centered cubic structure (fcc) containing relatively large carbide particles of the MC-type (M stands for metal such as W, Mo, Ti, Ta or a combination of these depending upon the exact chemical composition of the superalloy). Most of the γ′-phase, which assumes a cubical morphology is made to precipitate by a standard aging heat treatment defined for each alloy. However, additional γ′ with finer size and nearly spherical morphology is precipitated during cooling from the aging temperature and therefore, it is commonly referred to as cooling γ′ [4]. A distinctive feature of the cubical particles of γ′-phase is that they maintain high coherency with the matrix γ-phase. Therefore, the associated coherency strain provides an important source of strengthening. Additional strengthening is also provided by the cooling γ′-phase particularly at lower temperatures [8].

According to design specifications, the life expectancy of turbine blades used in industrial applications ranges from 35,000 to 100,000 h depending upon the engine type, operating conditions, and material systems selected for the application [7]. Although every effort is made to eliminate or minimize the incidents of unscheduled shutdowns and reduce maintenance costs, various types of damage leading to premature failure can still occur due to the combined effects of high temperatures, mechanical stresses and environmental conditions, e.g., [8–15]. In the meantime, because of the initial high material and processing costs, refurbishing of used blades is a common practice to re-qualify damaged blades for service. Various repair techniques have been devised particularly those based upon advanced welding technology [16–18].

Since the superalloys are complex multi-component alloy systems, their initial microstructures prior to service exist in state of metastable equilibrium. Subsequent exposure at elevated temperatures during service can lead to significant changes in microstructure, which can have detrimental effects on properties. Therefore, there has been an increasing interest in developing heat treatment schedules capable of restoring most of the initial microstructural features and properties [19,20]. It is then important to develop an in-depth understanding of the types of microstructural changes and associated degradation modes under actual service conditions [20]. Toward that objective, the present study has been undertaken to emphasize the important role of detailed microstructural characterization in identifying the various degradation modes of turbine blades exposed to service conditions.

2. Materials and experimental methods

First-stage turbine blades made of Udimet® alloys 520, 720, and 710 are included in the study (®Udimet is a registered trademarks of Special Metals Corporation group of companies). Table 1 shows their nominal chemical compositions as well as the compositions of the respective alloy heats included in the study as measured by inductively coupled plasma atomic-energy spectroscopy. All blades were coated with the same Cr-modified aluminide. The damaged blades were removed from different engines of the same model operating under the same conditions as per the design specifications listed in Table 2. For comparative purposes, samples of unused blades were also included in the study.

To reveal the grain structure of the superalloys, specimens were etched in a solution consisting of 80% hydrochloric acid by volume and 20% by volume of 15 mol% chromic acid. Various techniques used to characterize the microstructure included scanning electron microscopy (SEM) combined with energy dispersive X-ray spectroscopy, X-ray diffraction and analytical electron microscopy operating in the transmission and scanning transmission modes (TEM/STEM) combined with energy dispersive spectroscopy. Specimens for SEM were examined at 20 keV in the as-polished and etched conditions. Whenever applicable, oxidized fracture surfaces were descaled in HCl prior to SEM examination. X-ray diffraction experiments were carried out on polished specimens using Cu Kα radiation. Thin-foils for TEM/STEM were prepared by the jet polishing technique in a solution consisting of 30% nitric acid and 70% methanol by volume. All foils were examined at 200 keV.

Table 1
Chemical compositions in wt.%; nominal (measured).

Element	Udimet 520	Udimet 720**	Udimet 710
Ni	Balance (56.86)	Balance (58.07)	Balance (57.54)
Co	11–14 (13.70)	14.5–15.5 (14.97)	13–17 (15.12)
Cr	18–20 (19.32)	15.5–16.5 (15.10)	16–20 (18.87)
Al	1.8–2.3 (2.08)	2.25–2.75 (2.66)	2–3 (2.74)
Ti	2.9–3.25 (3.12)	4.75–5.25 (4.86)	4–6 (4.79)
Mo	2–4 (3.74)	2.75–3.25 (3.07)	2–4 (3.38)
W	0.8–1.2 (1.18)	1–1.5 (1.23)	1–2 (1.56)
Si	–	–	–
Mn	–	–	–
Fe	–	–	–
Zr	–	0.025–0.05 (0.04)	–
B	0.004–0.01 (ND)	0.01–0.02 (ND)	0.02* (ND)
C	0.02–0.06 (ND)	0.01–0.02 (ND)	0.07* (ND)

ND: not determined.
* Maximum.
** Low-Cr version.

Table 2
Blades history (all blades are coated with the same Cr-aluminide).

Blade alloy	Nominal temperature (°C)	Fuel	Life (h)	Condition
Udimet 520	800	Distillate oil	8100	Open crack
Udimet 720	800	Distillate oil	74,461	Fracture
Udimet 710	800	Distillate oil	1445	Fracture

3. Results and discussions

3.1. Microstructures of unused blades

Fig. 1 summarizes characteristic microstructural features of unused blade made of alloy 520. The gross grain structure is shown in the backscattered electron image of Fig. 1a. Primary MC carbide particles within the matrix phase and at grain boundaries are indicated by the arrows. A secondary electron SEM image illustrating the morphology of the γ′-phase is shown in Fig. 1b. The cubical γ′ particles precipitated by the aging heat treatment are observed to have a size ranging from about 0.5 to 1 μm. As can be seen from Fig. 1c, the finer cooling γ′ particles have a spherical morphology. Fig. 1d is a representative energy dispersive X-ray spectrum illustrating the elemental composition of the MC carbide observed in Fig. 1a. As can be seen, the composition of appears to be consistent with a carbide of the type $(Ti_{0.8}Mo_{0.2})C$ [4].

Typical microstructural features of unused blade made of alloy 720 are shown in Fig. 2. The cubical γ′-phase is shown in the bright-field STEM image of Fig. 2a with a size mostly less than 1 μm. A $\langle 001 \rangle_{fcc}$ microdiffraction pattern derived from the particle marked (x) is shown in the inset. Characteristic reflections of the $L1_2$ superlattice are observed at {100}, {110} and all equivalent positions. Similar to the case of alloy 520, the primary MC carbide shown in Fig. 2b and c appears to be of the type $(Ti_{0.8}Mo_{0.2})C$, however, it contains a small concentration of Zr as observed from the spectrum of Fig. 2d. As shown in Table 1, alloy 720 contains some Zr in contrast with alloy 520, which is Zr-free. Consistent with the composition of alloy 710 (Table 1), the primary MC carbide is found to be similar to that in alloy 520. A secondary electron SEM image illustrating

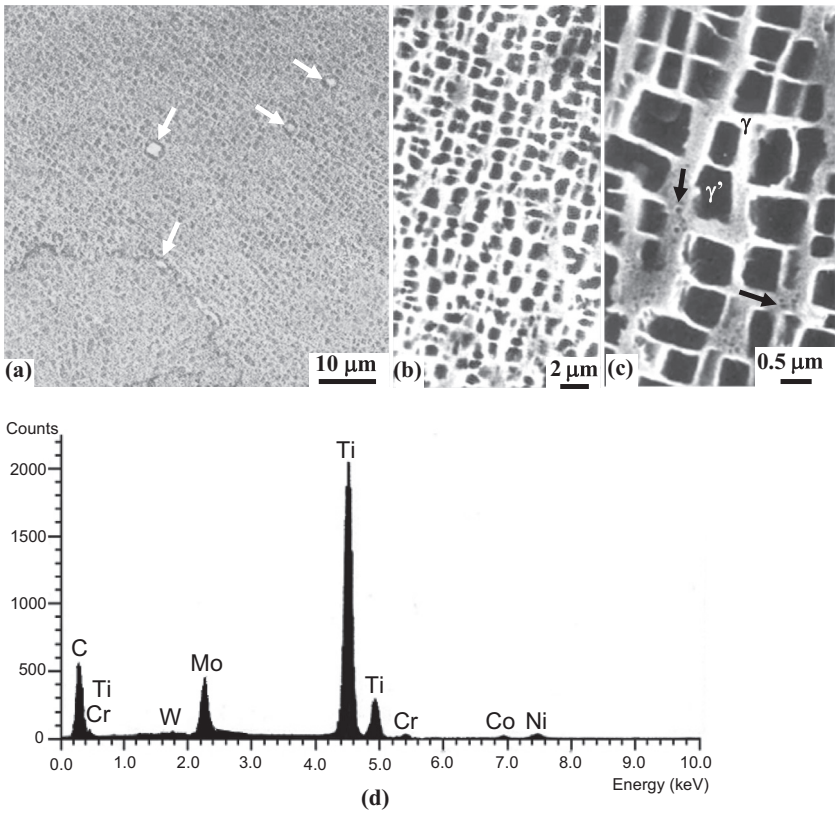

Fig. 1. Characteristic microstructure of unused blade made of alloy 520. (a) Backscattered electron image of the gross microstructural features; MC carbide particles are indicated by the arrows. (b) Secondary electron SEM image showing the microstructure of the cubical γ′-phase. (c) A magnified image showing the cooling γ′ as indicated by the arrows. (d) Energy dispersive spectrum illustrating the elemental composition of the MC carbide observed in (a).

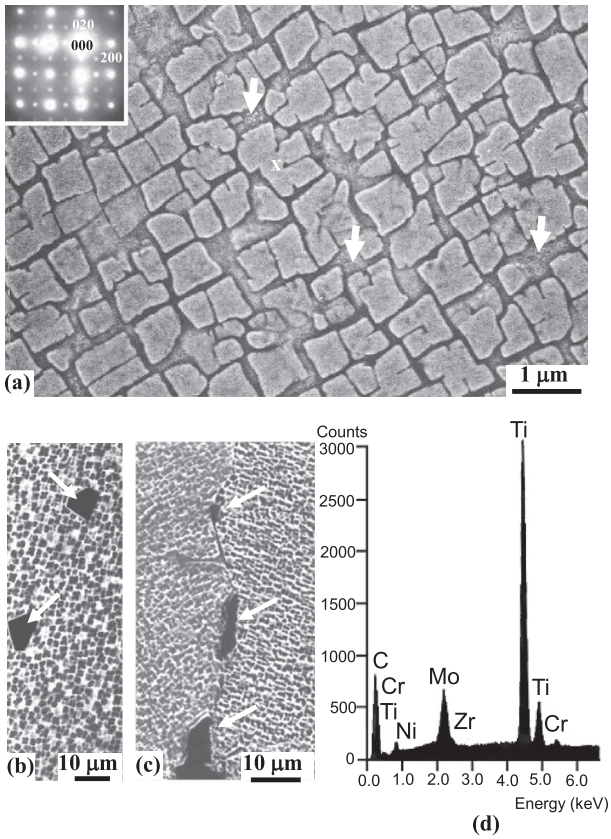

Fig. 2. Characteristic microstructure of unused blade made of alloy 720. (a) Bright-field STEM image of the cubical γ′-phase; the arrows point at the cooling γ′ and the inset is a microdiffraction pattern derived from the particle marked (x) in $\langle 001 \rangle_{fcc}$ orientation. (b) And (c) are secondary electron SEM images showing MC carbide particles in the matrix and at a grain boundary respectively. (d) Energy dispersive spectrum illustrating the elemental composition of the carbide observed in (b) and (c).

the morphology of γ′-phase in the blade made of alloy 710 is shown in Fig. 3. It is observed that the γ′ structure is rather coarser than that in the blades made of alloys 520 and 710. Also, the respective morphology is not quite cubical, which can be related to the relatively large particle size.

It is evident from the above results that among the three types of blades included in the study, the γ′-phase in the blade made of alloy 720 is observed to have the finest structure followed by the blades made of alloys 520 and 710 in order of

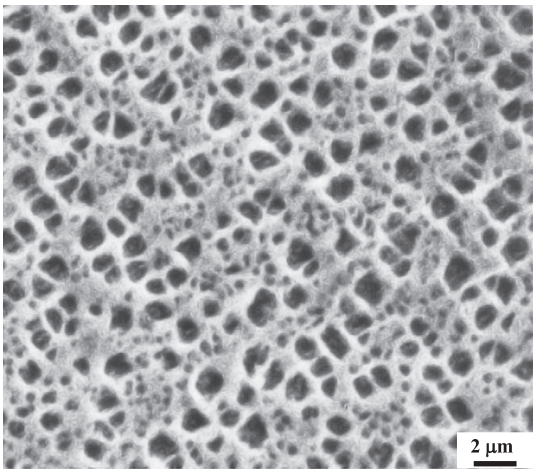

Fig. 3. Secondary electron SEM image illustrating the microstructure of the cubical and cooling γ′ in unused blade made of alloy 710.

coarser structures as demonstrated in Figs. 1–3. Also, alloy 720 is distinguished by its relatively lower Cr content and the presence of small concentration of Zr. These differences are found to be reflected on service performance as demonstrated later.

As an example, Fig. 4 summarizes typical microstructural features of the Cr-modified aluminide coating on the unused blade made of alloy 520. It is observed from the backscattered SEM image of Fig. 4a that the coating consists of two distinct zones followed by an interdiffusion zone (IDZ). The predominant constituent of zone I is α-Cr (body-centered cubic (bcc); $a = 0.2885$ nm) containing islands of β-phase based upon the NiAl composition (cubic B2-type superlattice; $a = 0.2887$ nm) as can be concluded from the X-ray diffraction of Fig. 4b and energy dispersive spectra of Fig. 4c and d. Since the lattice constants of α-Cr and β-NiAl are quite similar and because the disordered structure of β-NiAl is bcc, the characteristic reflections of the bcc structure of α-Cr coincide with the fundamental reflections of the ordered β-NiAl (Fig. 4b).

3.2. Macroscopic features of damaged blades

Due to the continuing demand for higher power, it is always required to use higher firing temperature. This results in higher blade surface temperature as well as higher temperature gradients. Therefore, the blades become more susceptible to degradation by creep, and fatigue, and oxidation [20]. However, higher than normal temperatures can also result from blockage of blade cooling passages by dust particles due to defective filters.

Photographs illustrating the extent of damage sustained by each blade are shown in Fig. 5. Except for a relatively thicker oxide layer on the fracture surface of the blade made of alloy 710, there has been no macroscopic evidence for corrosion attack suggesting that the damage sustained by the three blades is mostly of mechanical nature.

As illustrated in Fig. 5a and Table 2, the blade made of alloy 520 has developed an open crack at the leading edge after about 8100 h of operation. However, there has been no evidence for macroscopic deformation. It is observed from Fig. 5a that the crack has propagated along two distinct directions. At the edge of the blade, the crack has propagated along a direction oriented at about 45° to the direction of maximum tensile stress, which is typical of mode III fracture (shear or slant fracture) leading to the formation of a shear lip. Propagation is then observed to change into a direction normal to the direction of maximum tensile stress typifying mode I fracture (flat fracture). It is well known that slant fracture occurs in thin plates under plane stress condition and flat fracture occurs in thick plates under plane strain condition. Therefore, crack

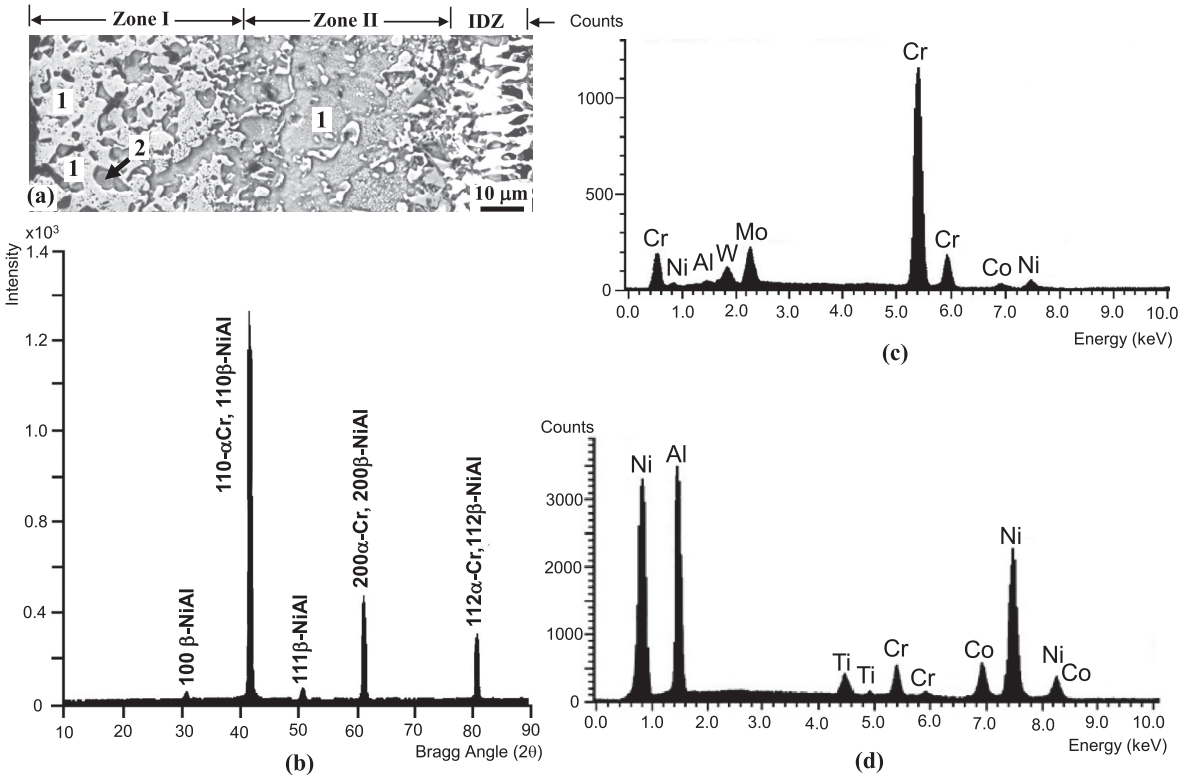

Fig. 4. An example derived from unused blade made of alloy 520 to illustrate the characteristic microstructural features of Cr-modified aluminide coating. (a) Backscattered SEM image along a cross-section of the coating and into the substrate. (b) X-ray diffraction pattern derived from the coating surface. (c) Energy dispersive spectrum illustrating the elemental composition of α-Cr in the outer coating layer (regions marked 1 in (a)). (d) Energy dispersive spectrum illustrating the elemental composition of β-phase (regions marked 2 in (a)).

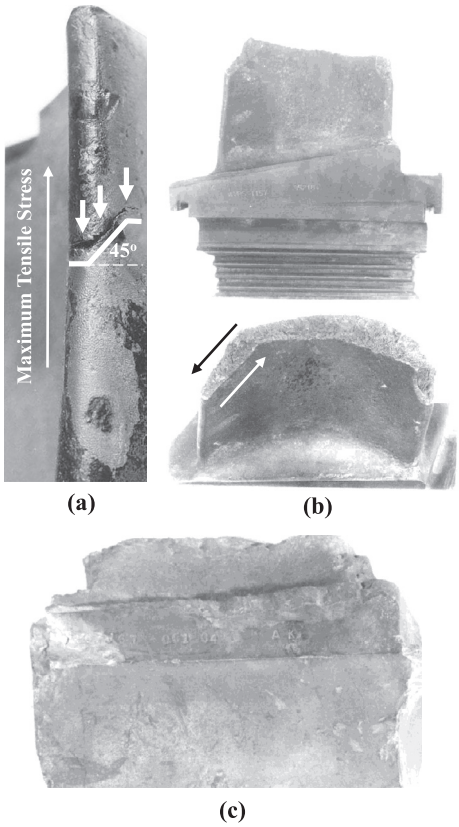

Fig. 5. Photographs illustrating the general appearance of used blades. (a) Blade of alloy 520 containing an open crack. (b) Fractured blade of alloy 720. (c) Fractured blade of alloy 710.

propagation by mixed mode I/III corresponds to a plate of intermediate thickness and can be produced by a combination of tension and torsion [21,22]. Such a change in crack propagation mode can result from variation in the stress distribution at the crack tip as well as the microscopic processes responsible for the fracture [23,24].

Fig. 5b shows the blade made of alloy 720, which has completely fractured by mixed mode I/III after 74,461 h of operation. Also in this case, there has been no evidence for noticeable macroscopic deformation. Another case of complete fracture is shown in Fig. 5c for the blade made of alloy 710. In this case, complete fracture has occurred after about 1844 h of operation. However, as observed in Fig. 5c, the blade has undergone extensive macroscopic deformation, which is indicative of higher than normal temperature.

A clue to the microscopic processes leading to the fractures observed in Fig. 5 is provided by microstructural characterization of the exposed fracture surfaces as described below. It is important to note here that any final fracture results from an overloading condition, however, crack propagation can occur by various mechanisms. Eventually, the load-bearing cross-section of the component is reduced to the extent corresponding to an overloading condition leading to final separation similar to the case of a conventional tensile test. Therefore, in order to reconstruct the microscopic sequence of events leading to fracture, it is important to have the entire fracture surface available for characterization.

3.3. Fracture behavior

Fig. 6 shows secondary electron SEM images illustrating the characteristic morphologies of the surfaces exposed by the crack of Fig. 5a (alloy 520). Fracture by microvoid coalescence is observed in the shear lip near the edge of the blade as illustrated in Fig. 6a. Although Fig. 6b shows that fracture in the flat region has occurred by intergranular separation, microvoid coalescence is observed at separated grain facets as illustrated in the inset similar to that observed in systems containing alloy-depleted zones alongside grain boundaries [25]. However, as further discussed later, intergranular separation can be aided by precipitation of secondary phases and microvoids at grain boundaries can also result from creep deformation. In addition to the macroscopic crack observed in the blade of Fig. 5a, secondary cracks are observed along cross-sections of the coating and into the superalloy substrate as illustrated in the example of Fig. 6c. It is observed that the crack has propagated in a straight path through the Cr-modified aluminide coating and to some extent through the superalloy

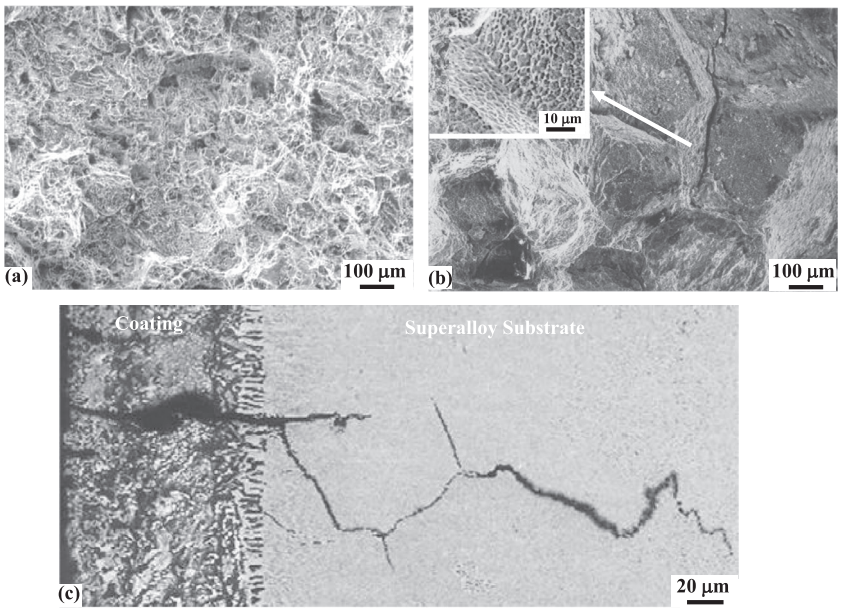

Fig. 6. Secondary SEM images illustrating the morphology of surfaces exposed by the open crack in Fig. 5a and secondary cracks. (a) Fracture by microvoid coalescence in the slant section (mode III). (b) Intergranular fracture in the flat section with microvoid coalescence in separated grain facets (mode I). (c) Secondary crack along the coating and into the superalloy substrate.

substrate and then assumed a zig-zag path indicative of propagation along grain boundaries. Crack propagation in straight path of coated superalloys is known to result from thermal fatigue [26]. It is noted here that the resistance to fatigue failure is known to be reduced by creep damage [27]. Cracks such as those shown in Fig. 6c can lead to spallation of the protective coating and provide an easy path for grain boundary oxidation as shown later. Also, it is noted from Fig. 6c that in comparison with the as-deposited condition (Fig. 4a) zones I and II of the coating have become indistinguishable, which can result from significant interdiffusion.

Qualitatively, the fracture behavior of the blade shown in Fig. 5b (alloy 720) is found to be similar to that of the blade shown in Fig. 5a except that there has been no evidence for visible fatigue cracks. As illustrated in the secondary electron SEM image of Fig. 7a, fracture in the shear lips has occurred by microvoid coalescence. Fig. 7b shows that fracture in the central flat region has occurred by an intergranular mechanism. Furthermore, intergranular cracks are observed along cross-sections of the blade as shown in the example of Fig. 7c. However, the respective blade lives (Table 2) indicate that crack propagation has occurred at a much slower rate in comparison with the blade made of alloy 520. Although this difference in behavior may be related to higher than normal temperature in the case of alloy 520, the characteristic composition of alloy 720 may have been a contributing factor as explained later.

The surface exposed by fracture of the blade shown in Fig. 5c (alloy 710) is found to be rather heavily oxidized as shown in Fig. 8a. However, some important features of the fracture surface could be revealed after descaling. Striations characteristic of fatigue failure are observed near the blade edge as shown in the example of Fig. 8b. However, as shown in the image of Fig. 8c, there is an indication of intergranular separation. This is confirmed by the observation of secondary intergranular cracks along cross-sections of the blade as shown in the example of Fig. 8d. As noted earlier, higher than normal temperature results in high temperature gradient enhancing thermal fatigue.

Since the useful life of the blade shown in Fig. 5b (alloy 720) lies within the life expectancy range, its failure is not considered to be premature. This can serve as a useful guide in planning a strategy to minimize the incidents of premature failure. As demonstrated below, the fracture behavior observed in Figs. 6–8 is correlated with changes in the initial microstructural features during exposure to service conditions.

3.4. Changes in morphology of the γ′-phase

Although in many cases, there can be no macroscopic evidence for overheating and/or deformation of turbine blades, microstructural characterization can provide very useful information by noting the changes in morphology of γ′-phase (size, shape and distribution). Microstructural characterization of the blades shown in Fig. 5 has revealed two major types of changes in the morphology of γ′-phase, which can degrade blade performance during service, namely: (i) coarsening, agglomeration and formation of rafts in the matrix γ-phase, and (ii) formation of γ′-denuded zones alongside grain boundaries due to precipitation of the Cr-rich $M_{23}C_6$ carbide. Examples of each type are given below.

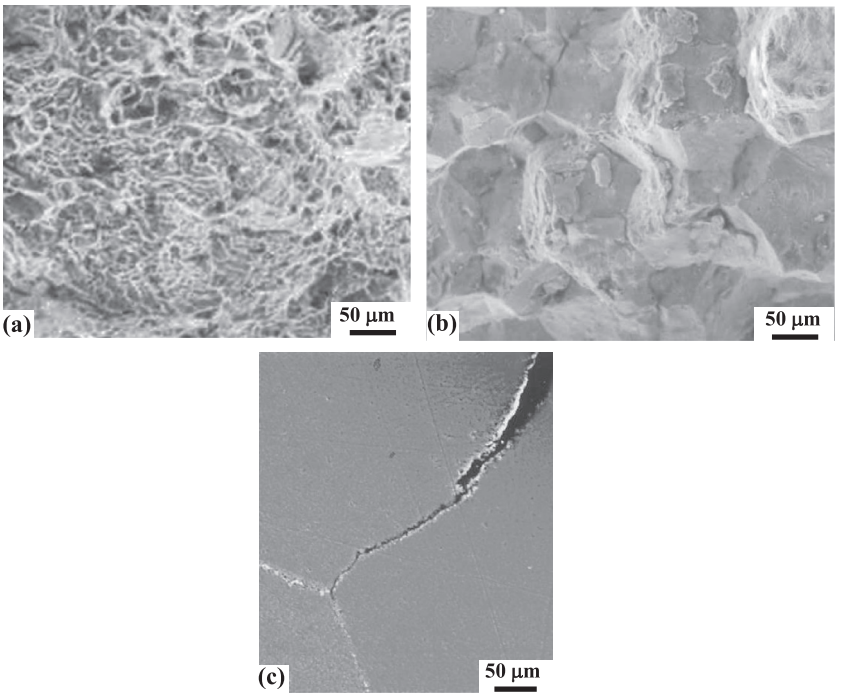

Fig. 7. Secondary SEM images illustrating the morphology of surface exposed by fracture of the blade in Fig. 5b and secondary cracks. (a) Microvoid coalescence in the slant section (mode I). (b) Intergranular fracture in the flat region (mode I). (c) Secondary intergranular crack along a cross-section of the superalloy substrate.

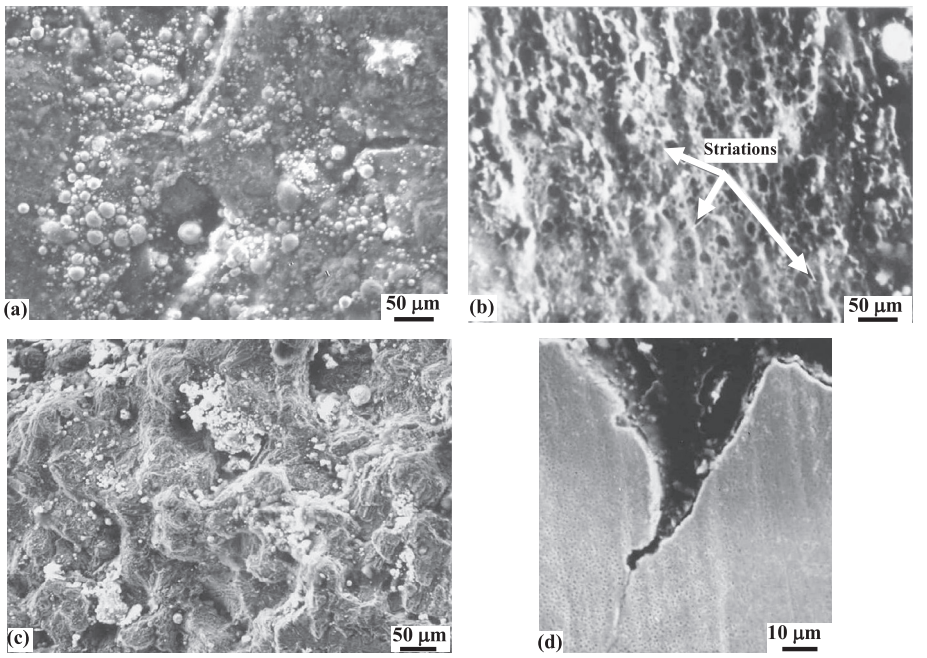

Fig. 8. Secondary SEM images illustrating the morphology of the surface exposed by fracture of the blade in Fig. 5c and secondary cracks. (a) Surface morphology prior to descaling. (b) Striations characteristic of fatigue fracture. (c) Intergranular fracture. (d) Secondary intergranular crack along a cross-section of the superalloy substrate.

3.4.1. Coarsening, agglomeration, and rafting of γ′-phase

According to the well known Ostwald ripening process, the γ′-microstructure in unused blade such as that shown in Fig. 1b is thermodynamically metastable. During exposure at elevated temperatures, larger particles tend to spontaneously

grow at the expense of smaller particles in order to reduce the surface energy of the system [28–30]. Fig. 9a shows a secondary electron SEM image illustrating the morphology of γ′-phase near the crack in the blade of Fig. 5a. It is observed that the microstructure becomes coarser in comparison with that of unused blade (Fig. 1b) leading to regions relatively free of γ′-phase and loss of the initial cubical morphology. As a result, coherency with the γ-phase is lost, which degrades the mechanical strength. Therefore, it becomes easier for dislocations to penetrate the γ′ particles as shown in the bright-field TEM image of Fig. 9b.

For the blades shown in Fig. 5b and c, the γ′-phase is observed to exhibit rafting morphology, which results from agglomeration and subsequent directional elongation of γ′ particles under the influence of the stresses generated by the high gas pressure [4]. Examples are given in Fig. 10. Rafting is known to occur at high temperatures in excess of about 0.8 Tm (Tm is the melting point in degrees K) or with prolonged exposure at lower temperatures [4]. Therefore, it is most likely that rafting in the blade of Fig. 5b has resulted from prolonged exposure at the operating temperature. In contrast, it is more likely that higher than normal temperature is the cause of rafting in the blade of Fig. 5c. This indicates that the temperature has exceeded 1000 °C which appears to be consistent with the macroscopic deformation observed in Fig. 5c and the oxidized fracture surface of Fig. 8a.

The above observations indicate that the blade made of alloy 520 has been subjected to moderately higher than normal temperature. However, it is evident that excessively higher than normal temperature is encountered in the case of the blade made of alloy 710. In contrast, the observed life of the blade made of alloy 720 demonstrates that the design specifications have been strictly followed during service. However, as noted earlier, it is also possible that the characteristic composition of alloy 720 has been a contributing factor. It is shown later, that this may be related to its relatively lower Cr content and the presence of a small concentration of Zr as shown in Table 1.

3.4.2. Precipitation of $M_{23}C_6$ carbide and formation of γ′-denuded zones alongside grain boundaries

Zones free of γ′-phase near the grain boundaries are observed in the three blades shown in Fig. 5. Although a number of models have been advanced to explain the mechanism responsible for formation of γ′-denuded zones, the zones observed in the present study are found to be consist with the model based upon localized Cr depletion due to grain boundary precipitation of the Cr-rich $M_{23}C_6$ carbide, which increases the solubility of Al and Ni in the γ-phase [4,31–34]. It is well

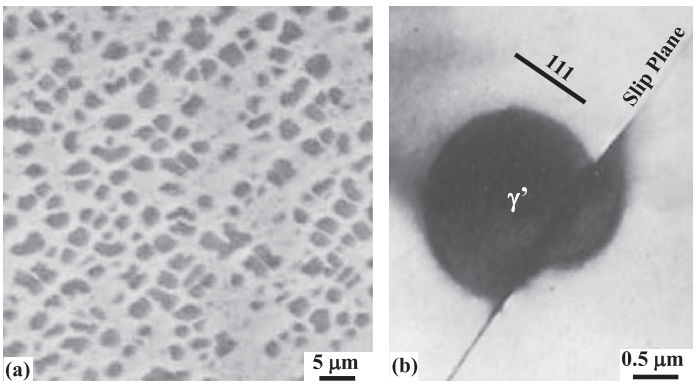

Fig. 9. Microstructure of γ′ phase in the used blade of alloy 520. (a) Secondary electron SEM image of coarsened γ′ particles in the matrix γ-phase. (b) Bright-field TEM image of a sheared γ′ particle.

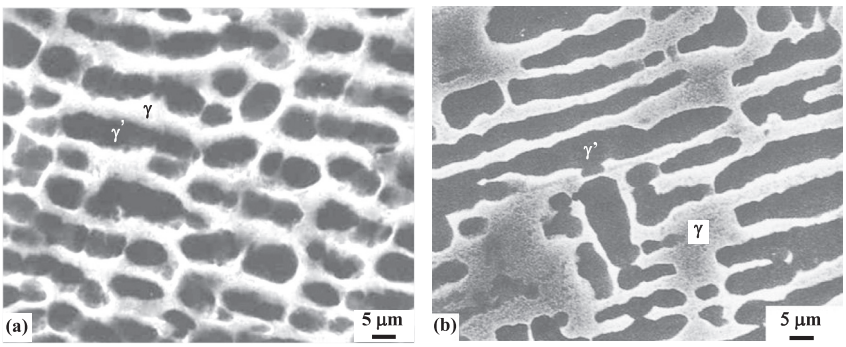

Fig. 10. Secondary electron SEM images illustrating rafting of γ′-phase in used blades of alloys 720 (a) and 710 (b).

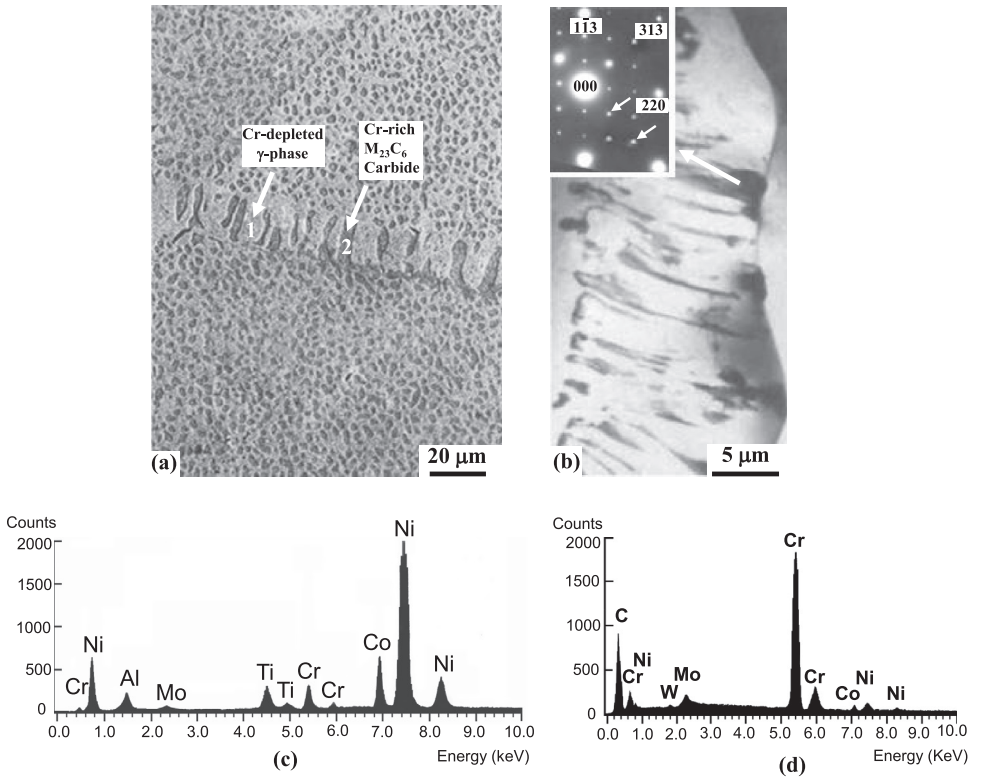

Fig. 11. Discontinuous grain boundary precipitation of Cr-rich $M_{23}C_6$ carbide in used blade of alloy 520. (a) Secondary electron SEM image illustrating lamellar carbide structure at a grain boundary. (b) Bright-field TEM image illustrating the lamellar carbide structure; the inset is a characteristic microdiffraction pattern of the carbide in $\langle \bar{3}32 \rangle_{fcc}$ orientation. (c) Energy dispersive spectrum derived from region 1 in (a). (d) Energy dispersive spectrum derived from region 2 in (a).

known that primary MC carbide such as that shown in Fig. 1a is thermodynamically metastable and tends to decompose into the more stable $M_{23}C_6$ carbide during exposure at elevated temperature [4].

At relatively low temperatures where precipitation of $M_{23}C_6$ carbide is more controlled by short-circuit diffusion along grain boundaries, the reaction occurs by a discontinuous mechanism resulting in characteristic lamellar or cellular morphology [35] such as that shown in the secondary electron SEM image of Fig. 11a, which is derived from a region away from the crack in the blade of Fig. 5a. As can be seen, the lamellar structure is distinguished from the matrix phase by being free of γ′ particles. Fig. 11b shows a bright-field STEM image of the lamellar grain boundary structure and corresponding microdiffraction pattern of the cubic carbide phase with fcc structure in $\langle \bar{3}32 \rangle_{fcc}$ orientation. It is typical of $M_{23}C_6$ carbide to have a lattice constant about three-times that of the γ-phase and therefore, it produces characteristic reflections at every one-third position of the γ-phase reflections [36] as observed in Fig. 11b. The energy dispersive spectra of Fig. 11c and d illustrate the elemental compositions of the regions marked 1 and 2 in Fig. 11a respectively. As can be seen, the elemental composition of region 1 is consistent with that of γ-phase, and the composition of region 2 is consistent with that of the carbide phase. Also, it is observed that the lamellar grain boundary structure is free of γ′ particles and that the lamellar regions of γ-phase are depleted in Cr. It is well known that a lamellar structure such as that shown in Fig. 11a is detrimental to creep-rupture life and ductility [31–35,37]. Furthermore, the Cr-depleted regions become susceptible to high oxidation rate.

For the blades shown in Fig. 5b and c, the $M_{23}C_6$ carbide is observed to have the morphology of a continuous grain boundary layer as shown in the backscattered SEM images of Fig. 12a and b and corresponding energy dispersive spectra. This observation indicates that the reaction has been more controlled by volume diffusion and therefore, it has occurred at a relatively higher temperature in comparison with the case shown in Fig. 11. Voids within the carbide precipitate at the grain boundaries can also be observed from Fig. 12a and b. Fig. 12c is an example derived from the blade of Fig. 5c to illustrate the γ′-denuded zone as viewed on the finer scale of TEM. The $M_{23}C_6$ carbide at the grain boundary and γ′-phase in the matrix are indicated by their characteristic microdiffraction patterns in $\langle 112 \rangle_{fcc}$ and $\langle 001 \rangle_{fcc}$ orientations respectively. Similar to the case of lamellar structure described above (Fig. 11), γ′-denuded zones such as those shown in Fig. 12 can have detrimental effects on mechanical strength [37].

It is evident from the above results that the stability of MC-type carbides toward decomposition into $M_{23}C_6$ carbide and the associated formation of γ′-denuded zones alongside grain boundaries can play an important role in limiting the useful life of turbine blades. As can be seen from Table 1, alloy 720 contains a small concentration of Zr, in contrast with the Zr-free

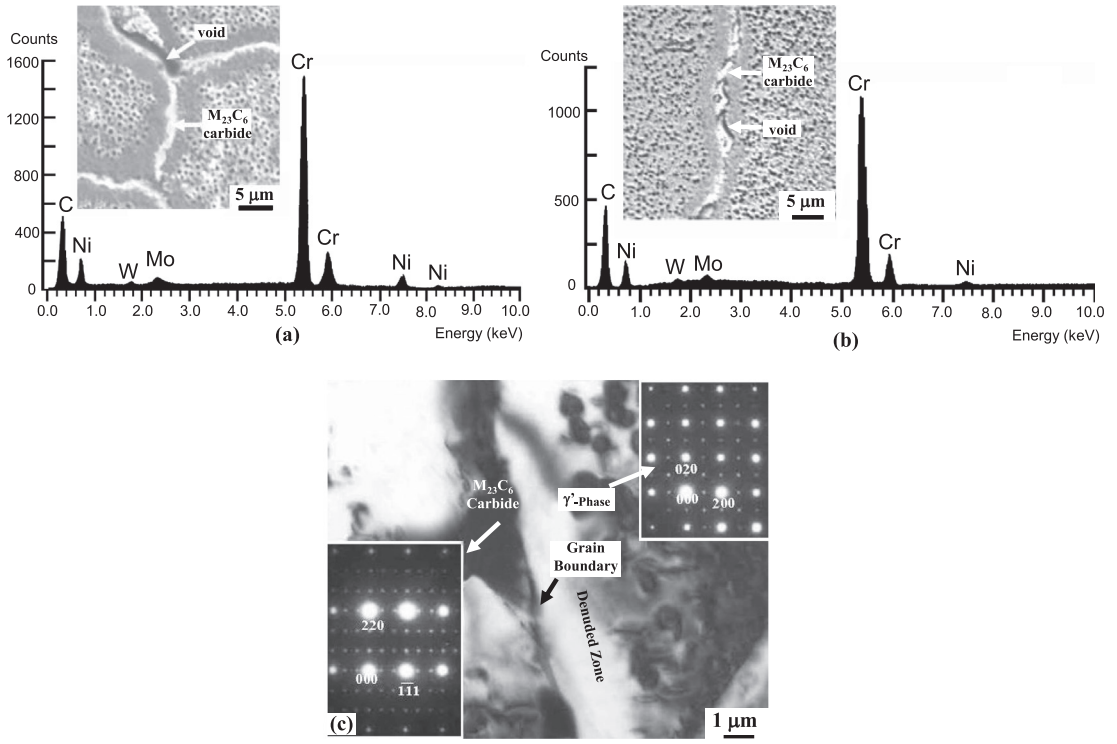

Fig. 12. Formation of γ′-denuded zones alongside grain boundaries containing continuous layers of $M_{23}C_6$ carbide in used blades made of alloys 720 and 710; grain boundary voids are indicated by the arrows. (a) Secondary electron SEM image and corresponding energy dispersive spectrum derived from the carbide phase in the blade made of alloy 720. (b) Secondary electron SEM image and corresponding elemental composition derived from the carbide phase in the blade made of alloy 710. (c) An example derived from the used blade 710 to illustrate the γ′-denuded zone as observed on the scale of TEM (bright-field TEM image and corresponding microdiffraction patterns of the $M_{23}C_6$ carbide and γ′-phase in $\langle 1\,1\,2\rangle_{fcc}$ and $\langle 0\,0\,1\rangle_{fcc}$ orientations respectively).

alloys 710 and 700. Also, it is observed from Fig. 3 that the MC carbide in alloy 720 contains some Zr. Since MC carbides are ranked as TaC, HfC, NbC, ZrC, TiC, WC, and MoC in order of decreasing stability [38,39], the MC carbide in alloy 720 is expected to have higher thermal stability in comparison with the carbides in alloys 710 and 700. Therefore, it is expected that decomposition of the MC carbide in alloy 720 proceeds with slower kinetics in comparison with alloys 520. Other beneficial effects of Zr are described later.

3.5. Creep damage and grain boundary oxidation

All three blades are found to sustain creep damage as reflected by the characteristic grain boundary cracks and cavitation. Fig. 13 shows an example derived from the blade of Fig. 5a. The secondary electron SEM image of Fig. 13a shows two modes for initiating intergranular creep failure: (i) wedge crack at a triple point, and (ii) cavities along the boundaries, which can form by coalescence of small voids. Fig. 13b shows the same region as viewed at higher magnification. Various studies have shown that grain boundary sliding plays an important role in forming the wedge cracks [40–44]. Also, some studies have shown that there is a link between the wedge cracks and cavities [40,42,43]. According to these studies, the wedge cracks result from accelerated linking of growing cavities by grain boundary sliding in the triple point region of stress concentration. Also, it has been shown that intergranular creep fracture can occur by coalescence of closely-spaced voids on grain boundaries oriented normal to the applied stress [40], which corresponds to mode I fracture. In this case, voids are observed at separated grain facts of the fracture surface [43] similar to that shown in Fig. 6b. This mode of creep fracture typically occurs at temperatures below about 0.75 Tm [44]. It has also been suggested that grain boundary precipitates including carbides and intermetallic phases can act as preferred sites for nucleation of voids [14,15,40] as demonstrated in Fig. 12a and b for the case of $M_{23}C_6$ carbide. Moreover, highly localized deformation in the soft γ′-denuded zones alongside grain boundaries can lead to formation of voids at the grain boundaries [37,40].

Fig. 14 shows an example derived from the blade of Fig. 5c to illustrate grain boundary oxidation induced by cracks produced by creep deformation. The secondary electron SEM images of Fig. 14a and b shows the respective oxide morphology as viewed at different magnifications. Fig. 14c is an energy dispersive spectrum derived from the region marked (x) in Fig. 14b. It is evident that the elemental composition of the oxide is consistent with that of Cr_2O_3. This type of internal oxidation is commonly referred to as stress-assisted intergranular oxidation [45].

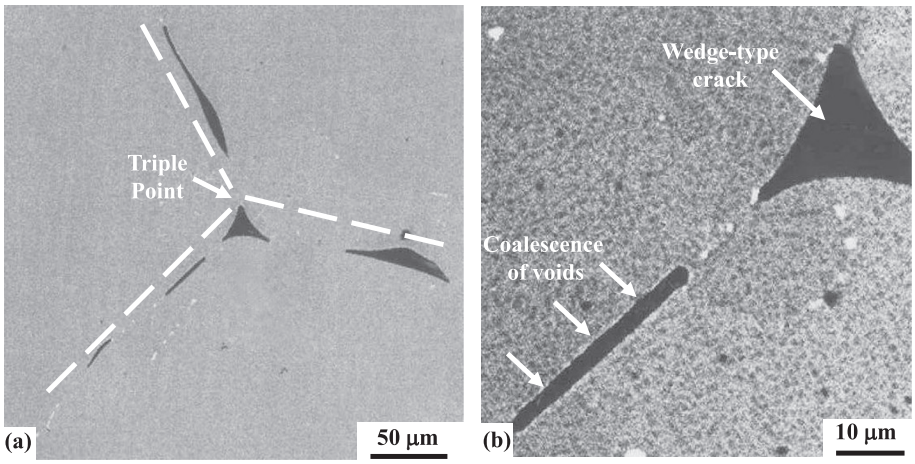

Fig. 13. Backscattered electron SEM images illustrating creep damage in used blade made of alloy 520. (a) Wedge crack at a triple point and cavities at grain boundaries. (b) Same region as viewed at higher magnification.

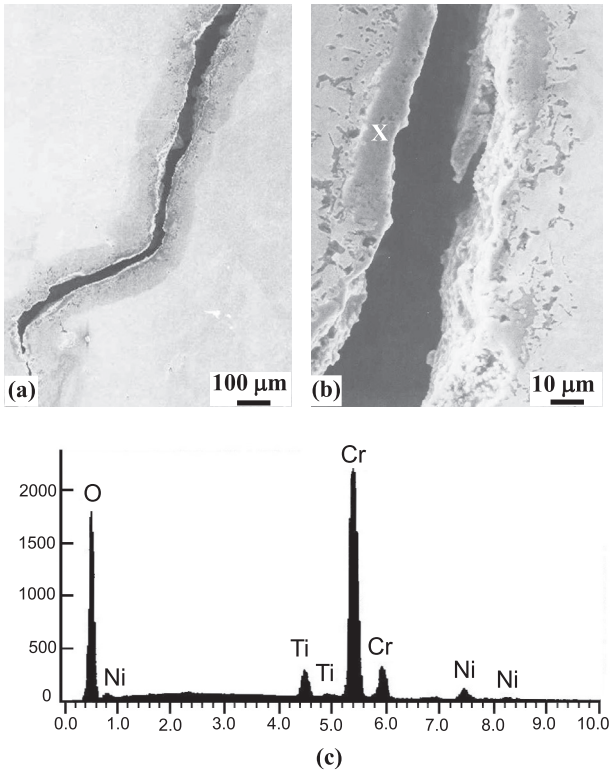

Fig. 14. Intergranular oxidation alongside cracks produced by fatigue/creep in used blade of alloy 710. (a) Low-magnification secondary electron SEM image illustrating the oxide layer alongside the crack. (b) Higher magnification image showing the oxide morphology. (c) Energy dispersive spectrum illustrating the elemental composition of the oxide.

3.6. Precipitation of intermetallic compounds

Because of their characteristic layered structures, intermetallic compounds precipitated in superalloys are usually referred to as topologically close-packed phases. Examples include the σ- and η-phases among others. These phases are well known to have detrimental effect on mechanical strength of the superalloy due to their extreme hardness and brittleness, e.g., [2,3,46,47]. In contrast with alloys 710 and 700, the low-Cr version of alloy 720 is characterized by high thermal stability and mechanical strength up to a temperature of about 925 °C [48–50]. This is reflected by the resistance

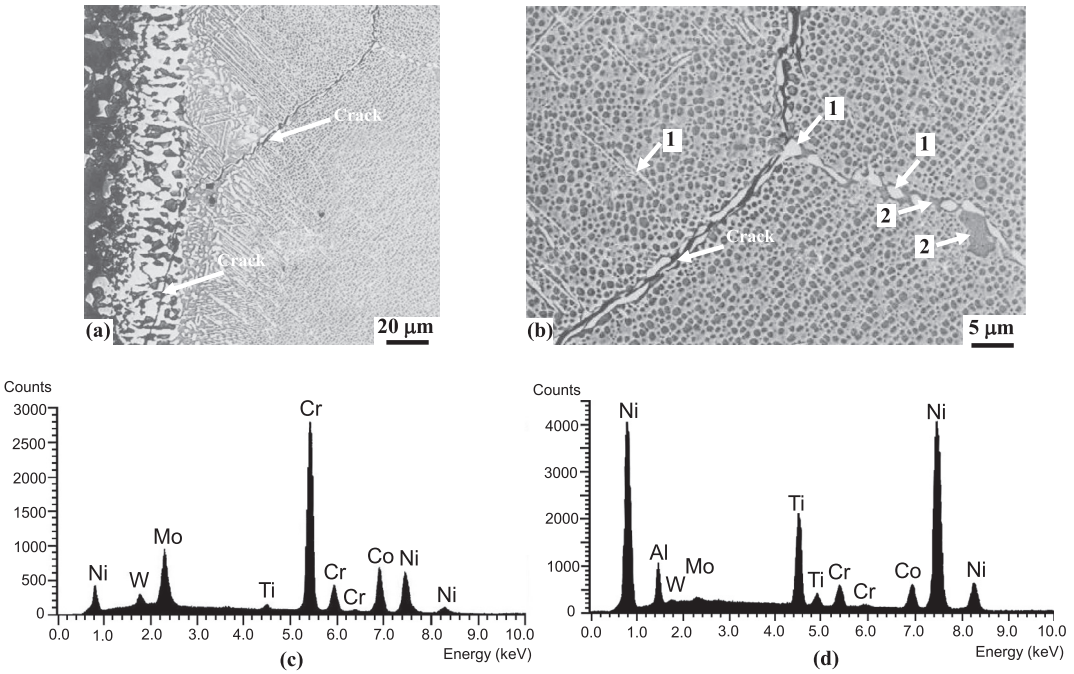

Fig. 15. Precipitation of intermetallic compounds in used blade made of alloy 520. (a) Low-magnification backscattered image showing continuous layers of grain boundary precipitates and matrix precipitates with platelet-type morphology. (b) High magnification image showing two phases at the grain boundaries. (c) Energy dispersive spectrum illustrating the elemental composition of the precipitates marked 1 at the grain boundaries and matrix phase in (b). (d) Energy dispersive spectrum illustrating the elemental composition of the grain boundary precipitates marked 2 in (b).

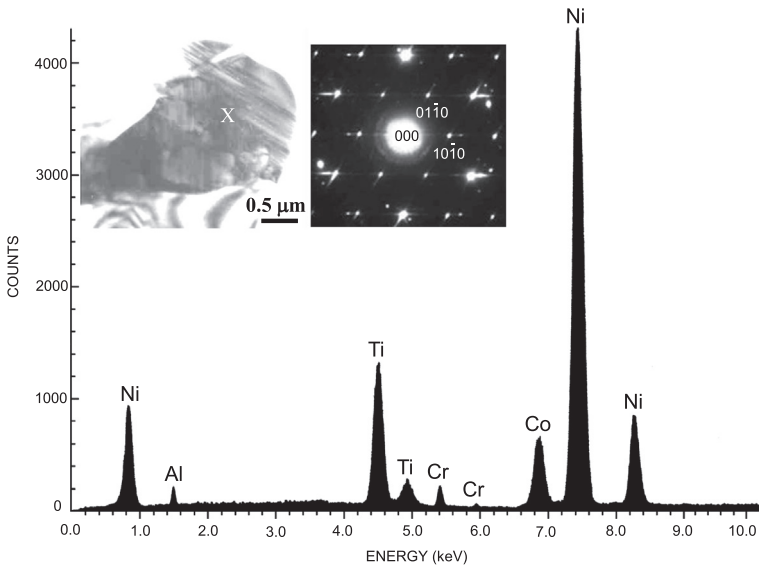

Fig. 16. Bright-field STEM image, corresponding microdiffraction pattern in $[0001]_{hcp}$, and energy dispersive spectrum illustrating a precipitate particle of η-phase (Ni_3Ti) in the blade made of alloy 720.

of the alloy to precipitation of detrimental intermetallic compounds particularly the σ-phase as well as the relatively high solvus temperature of the γ′-phase due to the lower Cr content [47,48]. Another factor contributing to the high performance of the alloy is the presence of a small concentration of Zr. It is well known that small additions of Zr to Ni-base superalloys can significantly improve their resistance to both creep and fatigue [51,52]. Although the corresponding effects on microstructure are not well established, there is an indication that Zr tends to segregate at grain boundaries and

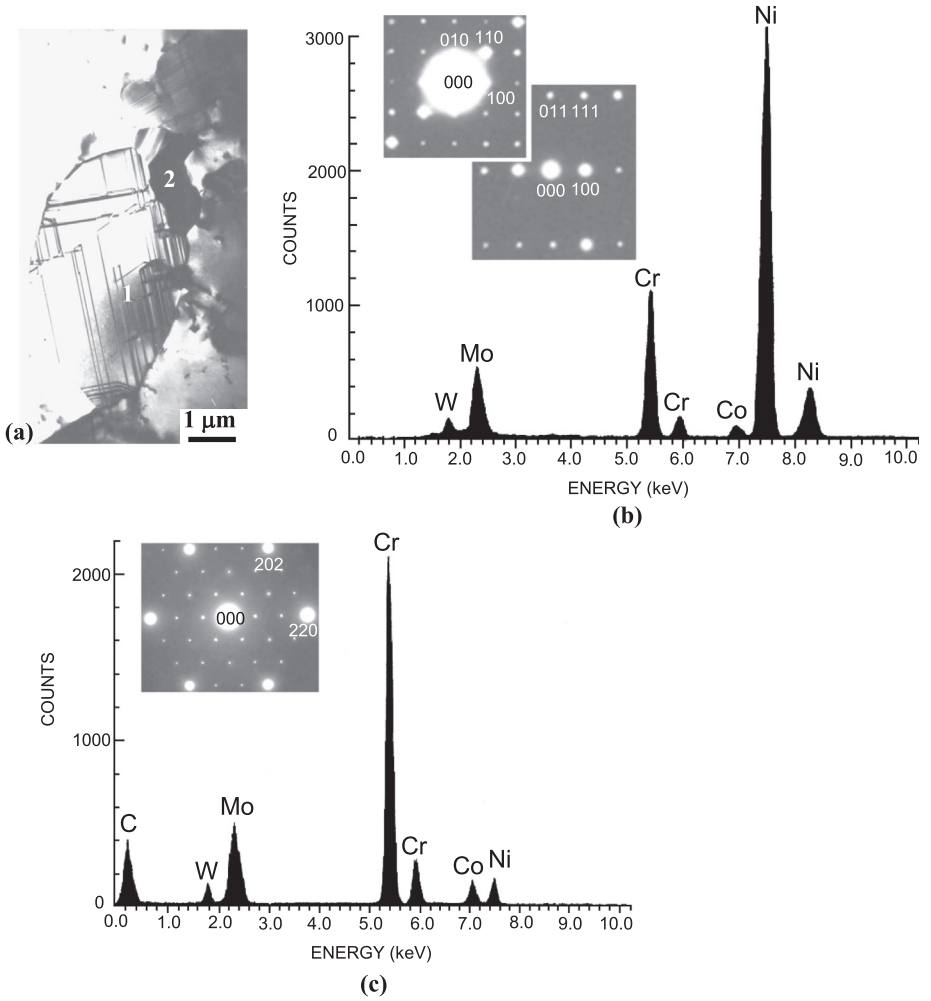

Fig. 17. Precipitation of σ-phase in the blade made of alloy 710. (a) Bright-field TEM image of grain boundary precipitates. (b) Microdiffraction patterns and energy dispersive spectrum derived from the particle marked 1 in (a). (c) Microdiffraction pattern and energy dispersive spectrum derived from the particle marked 2 in (a).

improve their cohesive strength and also reduces the susceptibility to precipitation of topologically close-packed phases such as the Laves phase and σ-phase [53].

Precipitates of both the σ- and η-phases have been identified in the blade made of alloy 520 as summarized in Fig. 15. Backscattered electron images illustrating intermetallic precipitates at grain boundaries and in the matrix phase are shown in Fig. 15a and b. Also, a continuous grain boundary crack is observed to extend through the coating. Corresponding energy dispersive spectra illustrating the elemental compositions of the precipitates are shown in Fig. 15c and d suggesting the presence of both σ-phase of the type (Ni + Co)–Cr–(Mo + W) and η-phase based upon the Ni_3Ti composition.

Also, η-phase has been identified by TEM/STEM analysis in the blade made of alloy 720 as shown in the example of Fig. 16. An η-phase particle suspended from the edge of a thin-foil is shown in the bright-field TEM image. The corresponding microdiffraction diffraction pattern in $[0\,0\,0\,1]_{hcp}$ orientation is consistent with the hexagonal DO_{24}-type structure of η-phase ($a = b = 0.25$ nm, $c = 0.83$ nm). Also, the corresponding energy dispersive shows that the elemental composition is consistent with that of Ni_3Ti. Fine striations observed in the Ni_3Ti particle are interpreted as stacking faults and fine twins. Evidently, precipitation of η-phase in the blade made of alloy 720 has occurred with sluggish kinetics.

An example illustrating a mixture of $M_{23}C_6$ carbide and σ-phase at a grain boundary in the blade made of alloy 710 is shown in the bright-field TEM image of Fig. 17a. Fig. 17b shows two microdiffraction patterns derived from the particle of σ-phase in [001] and [$0^{-}11$] tetragonal orientations and corresponding energy dispersive spectrum illustrating its elemental composition. Fig. 17c shows a microdiffraction pattern in $\langle 1\,1\,1\rangle_{fcc}$ orientation and corresponding energy dispersive spectrum consist with those of $M_{23}C_6$ carbide. It is known that pre-precipitation of the Cr-rich $M_{23}C_6$ carbide can act as a nucleus for precipitation of the Cr-rich sigma phase [47], which can explain the link between the two particles observed in Fig. 17a.

4. Conclusion

It is concluded from this study that selected turbine blades used in power generation and made of different Ni-base superalloys are susceptible to similar microstructural changes, which can degrade their performance leading to intergranular creep failure. In addition to creep failure, the blades can also become susceptible to fatigue failure particularly in those cases where higher than normal temperature is encountered during service. Detrimental changes in microstructure include coarsening, agglomeration, and rafting of the γ'-phase, formation of γ'-denuded zones alongside grain boundaries, and precipitation of intermetallic compounds particularly σ- and η-phases. However, the kinetics of these changes can vary from one case to another depending upon the exact operating temperature and superalloy composition used in the application. The results show that the life expectancy of the blades can be realized by appropriate material selection and adherence to design specifications.

Acknowledgements

The authors would like to acknowledge the support provided by King Abdulaziz City for Science and Technology (KACST) through the Science & Technology Unit at King Fahd University of Petroleum & Minerals (KFUPM) for funding this work through project No. 12-ADV2398-04 as part of the National Science, Technology and Innovation Plan.

References

[1] Boyce MP. The gas turbine handbook. Oxford: Elsevier Science and Technology; 2012.
[2] Durand-Charre M. The microstructure of superalloys. London: Gordon and Breach Science Publishers; 2003.
[3] Donachie MJ, Donachie SJ. Superalloys: a technical guide. Materials Park: ASM International; 2002.
[4] Ross ER, Sims CT. Nickel-base alloys. In: Sims CT, Hagel WC, Stoloff NS, editors. Superalloys II. New York: Wiley; 1987. p. 97–133.
[5] Bose S. High temperature coatings. Oxford: Butterworth-Heinemann; 2007.
[6] Wood JH, Goldman E. Protective coatings. In: Sims CT, Hagel WC, Stoloff NS, editors. Superalloys II. New York: Wiley; 1987. p. 359–84.
[7] Morocutti O. A guide to the control of high temperature corrosion and protection of gas turbine materials. Brussels: Commission of the European Communities; 1986.
[8] Bernstein H. Materials issues for users of gas turbines. ASME Technical Paper No. T3504, New York: ASME; 2006.
[9] Carter TJ. Common failures in gas turbine blades. Eng Fail Anal 2005;12:237–47.
[10] Qu S, Fu CM, Dong C, Tian JF, Zhang ZF. Failure analysis of the 1st stage blades in gas turbine engine. Eng Fail Anal 2013;32:292–303.
[11] Pokluda J, Kianicova M. Assessment of performance capability of turbine blades with protective coatings after overheating events. Eng Fail Anal 2010;17:1389–96.
[12] Huda Z. Metallurgical failure analysis for a blade in a gas-turbine engine of a power plant. Mater Des 2009;30:3121–5.
[13] Tawancy HM, Al-Hadhrami LM. Degradation of turbine blades and vanes by overheating in a power station. Eng Fail Anal 2009;16:273–80.
[14] Tawancy HM, Al-Hadhrami LM. Failure of refurbished turbine blades in a power station by improper heat treatment 2009;16:810–5.
[15] Tawancy HM, Al-Hadhrami LM. Application of microstructural characterization and computational modeling. Eng Fail Anal 2008;15:1027–34.
[16] Zheng JM, Li ZG, Chen X. Worn area modeling for automating the repair of turbine blades. Int J Adv Manuf Tech 2006;29:1062–7.
[17] Dodd A, Bialach J. Laser's repair of turbine blades. Weld J 2003;82:42–5.
[18] Pascal C, Martin-Ayral RM, Tedenac JC, Merlet C. Combustion synthesis: a new route for repair of gas turbine components-achievements and perspectives for development of SHS rebuilding. J Mater Proc Technol 2003;135:91.
[19] Wangyao P, Krongtong V, Panich N, Chuankerkkul N, Lothongkum D. Effect of 12 heat treatment conditions after HIP process on microstructural refurbishment in cast nickel-based superalloy GTD-111. High Temp Mater Proc 2007;26:151–9.
[20] Daleo JA, Ellison KA, Boone DH. Metallurgical consideration for life assessment and requalification of gas turbine blades. J Eng Gas Turbines Power 2002;124:571–9.
[21] Lan W, Deng X, Sutton MA, Cheng C-S. Study of slant fracture in ductile materials. Int J Fract 2006;141:469–96.
[22] Ebrahimi F, Liscano AJ. Microstructure/mechanical properties relationship in electrodeposited Ni/Cu nanolaminates. Mater Sci Eng A 2001;A301:23–34.
[23] Broek D. Fracture mechanics as an important tool in failure analysis. In: Dickson JI, Abramovici E, Marchand NS, editors. Failure analysis techniques and applications. Materials Park: ASM International; 1992. p. 33–44.
[24] Broek D. The practical use of fracture mechanics. Norwell: Kluwer Academic Publishers; 1989.
[25] Burghard HC. The influence of precipitate morphology on microvoid growth and coalescence in tensile fractures. Met Trans 1974;5:2083–94.
[26] Santhanam AT, Beck CG. The influence of protective coatings on thermal fatigue resistance of Udimet 710. Thin Sol Films 1980;73:387–95.
[27] Hou J, Wicks BJ, Antoniou RA. An investigation of fatigue failure in turbine blades by mechanical analysis. Eng Fail Anal 2002;9:201–11.
[28] Lifshitz IM, Slyozov VV. The kinetics of precipitation from supersaturated solid solutions. J Phys Chem Solid 1961;19:35–50.
[29] Baldan A. Progress in Ostwald ripening theories and their applications to nickel-base superalloys Part I: Ostwald ripening theories. J Mater Sci 2002;37:2171–202.
[30] Baldan A. Progress in Oswald ripening theories and their applications to the γ'-precipitates in nickel-base superalloys. J Mater Sci 2002;37:2379–405.
[31] Wolfenstine J, Ruano OA, Wadsworth J, Sherby OD. Refutation of the relationship between denuded zones and diffusion creep. Scr Metall Mater 1993;29:515–20.
[32] Tien JK, Gamble RB. Influence of applied stress and stress sense on grain boundary precipitate morphology in a nickel-base superalloy during creep. Met Trans 1971;2:1663–7.
[33] Ashby MF, Palmer IG. The dragging of solid particles through metals by grain boundaries. Acta Metall 1967;15:420–3.
[34] Tavassoli A, Colombe G. Mechanical and microstructural properties of alloy 800. Metall Trans 1978;9:1203–11.
[35] Williams DB, Butler EP. Grain boundary discontinuous precipitation reactions. Int Met Rev 1981;26:153–83.
[36] Edington JW. Typical electron microscope investigations. Eindhoven: N.V. Philips; 1976.
[37] Floreen S. Mechanical properties. In: Sims CT, Hagel WC, Stoloff NS, editors. Superalloys II. New York: Wiley; 1987. p. 241–62.
[38] Mark HE, Othmer DF, Overberger CG, Seaborg GT. Encyclopedia of chemical technology. 3rd ed. New York: John Wiley; 1978.
[39] Toth LE. Transition metal carbides and nitrides. New York: Academic Press; 1971.
[40] Kassner ME, Hayes TA. Creep cavitation in metals. Int J Plasticity 2003;19:1715–48.
[41] Wadsworth J, Ruano OS, Sherby OD. Denuded zones, diffusional creep, and grain boundary sliding. Metall Mater Trans A 2002;33A:219–29.
[42] Shewmon P, Anderson P. Void nucleation and cracking at grain boundaries. Acta Mater 1998;46:4861–72.
[43] Chen IW, Argon AS. Creep cavitation in 304 stainless steel. Acta Met 1981;29:1321–31.

[44] Crossman FW, Ashby MF. Nonuniform flow of polycrystals by grain boundary sliding accommodated by power law creep. Acta Met 1975;23:425–40.
[45] Selvig A, Huang XA, Hildebrand M, Stek D. Investigation of stress assisted grain boundary oxidation cracking in MAR-M002 high pressure turbine blades. J Eng. Gas Turbines Power Trans ASME 2011;133. article no. 082101.
[46] Sims CT. Prediction of phase composition. In: Sims CT, Hagel WC, Stoloff NS, editors. Superalloys II. New York: Wiley; 1987. p. 217–48.
[47] Wallork G, Croll J. A review of the strengthening mechanisms in iron and nickel-based Fe–Ni–Cr alloys. In: Newkirk, editor. Reviews of high temperature materials. London: Freund Publishing House; 1976. p. 69–138.
[48] Udimet 720 alloy data brochure. Publication No. SMC-106. Huntington: Special Metals Corporation; 2004.
[49] Lindsley B, Pierron X. Sub-solvus recrystallization mechanisms in Udimet alloy 720Li. In: Pollock TM, Kissinger RD, Bowman, Green KA, McLean M, Olson S, Schirra JJ, editors. Superalloys 2000. Materials Park: TMS; 2000. p. 59–68.
[50] Reed RC, Jackson MP, Na YS. Characterization and modeling of the precipitation of the sigma phase in Udimet 720 and Udimet 720Li. Metall Mater Trans A 1999;30A:521–33.
[51] Huang HE, Koo CH. Effect of zirconium on microstructure and mechanical properties of cast fine-grain CM247 LC superalloy. Mater Trans 2004;45:554–61.
[52] Floreen S, Davidson JM. The effects of B and Zr on the creep and fatigue crack growth behavior of a Ni-base superalloy. Met Trans A 1983;14A:895–901.
[53] Yamin L, Hongjun L, Jie L, Zhipeng W, Yuan H. Effect of Zr addition on precipitates in K4169 superalloy. China Foundary 2012;9:6–12.